A Hybrid Modulation Strategy Providing Lower Inductor Current for the DAB Converter With the Aid of DC Blocking Capacitors

Peng Liu and Shanxu Duan, *Senior Member, IEEE*

***Abstract*—For the dual active bridge converter, the single phase shift (SPS) modulation strategy is simple and effective for controlling the transmission power. However, when the voltage varies widely, it is hard to realize soft switching and the circulating power increases dramatically, which results in the increased current stress and reduced efficiency. Thus, a hybrid modulation strategy is proposed in this article, whose main idea is to introduce a voltage offset across the dc blocking capacitors in both sides, and the converter can switch between different operating modes to lower the inductor current according to different operating conditions. Operational principle of the proposed modulation is introduced, and the normalized root-mean-square values of the inductor current in different working modes are derived mathematically, which leads to the selection criterion among different operating modes. The proposed scheme retains the simplicity of the conventional SPS strategy and improves the efficiency over wide voltage range and wide load range without complicating the topology structure. Finally, the performance of the proposed modulation is verified by the experimental results.**

***Index Terms*—Dual active bridge (DAB), dc blocking capacitor, hybrid modulation, inductor current reduction.**

I. INTRODUCTION

THE dual-active-bridge (DAB) converter was originally presented in [1], since then, the DAB converter and its variants (three-phase DAB [2], current-fed DAB [3], three-level DAB [4], [5], etc.) have been widely studied in the isolated dc−dc conversion area [6], [7]. Lately, due to its advantages such as galvanic isolation at high frequency and bidirectional power flow, DAB has become a promising interface for solid-state transformers [8], electric vehicles (EV) [9], medium-voltage direct current [10], [11] grids, etc.

As for the modulation technique, the conventional strategy is the single phase shift (SPS) modulation, which is known to be simple and effective for controlling the amplitude and direction of the power delivered by the DAB converter. When a DAB is connected to the battery of an uninterruptible power supply, EV, or energy storage device, the input or output voltage of the converter varies widely; therefore, a large amount of reactive power will be generated and the zero-voltage switching (ZVS) is hard to realize, which not only reduces the system efficiency but also dramatically increases the current stress of the switches.

In order to improve the performance of the DAB converter over wide voltage range and wide load range, one modulation method extended from SPS is to lower the duty cycle of the full bridge to below 50%. The resulting schemes are referred to as extended phase shift modulation [12], dual phase shift modulation [13], and triple phase shift modulation [14], which can help the DAB achieve lower current stresses [15] and an improved overall efficiency [16]. However, because of more control degrees to tune, the implementation of these advanced modulation strategies usually adopts complex mathematical analysis tool [15], which is significantly tougher than SPS. In contrast, SPS only needs a PI or other regulator to generate a proper phase-shifted angle from the output voltage or current error, depending on the applications. A variable switching frequency modulation technique was proposed in [17], which retains the simplicity of SPS, but a variable switching frequency will increase complexities associated with electromagnetic interference filter design. Moreover, under light load conditions, the switching frequency may also become extremely high to guarantee soft switching.

In order to retain the use of a fixed switching frequency SPS strategy, some researchers have explored different topology structures for efficiency improvement over wide voltage range and wide load range. A reconfigurable stacked active bridge converter was proposed in [18], which comprises a double stacked bridge inverter coupled with a reconfigurable rectifier through a three-winding transformer. The proposed converter can work in the low-power mode that improves light-load efficiency by extending the ZVS range and reducing the core loss. A similar structure was proposed for the resonant DAB converter in [19], which introduces two additional switches in the secondary side to switch the operation modes between full-bridge and half-bridge, thus the converter can achieve high efficiency throughout a wide range of operation voltage. Another reconfigurable three-level structure was proposed in [20], which also switches operation modes between full-bridge and half-bridge to reduce circulating current and reactive power for efficiency enhancement.

Manuscript received May 1, 2019; revised July 19, 2019; accepted August 20, 2019. Date of publication August 22, 2019; date of current version January 10, 2020. This work was supported in part by the National Key Research and Development Program of China under Grant 2018YF0106300 and in part by the China Postdoctoral Science Foundation under Grant 2018M640698. Recommended for publication by Associate Editor J. Biela. *(Corresponding author: Peng Liu.)*

The authors are with the State Key Laboratory of Advanced Electromagnetic Engineering and Technology, School of Electrical and Electronic Engineering, Huazhong University of Science and Technology, Wuhan 430074, China (e-mail: pliu0901@hust.edu.cn; duanshanxu@hust.edu.cn).

Color versions of one or more of the figures in this article are available online at http://ieeexplore.ieee.org.

Digital Object Identifier 10.1109/TPEL.2019.2937161

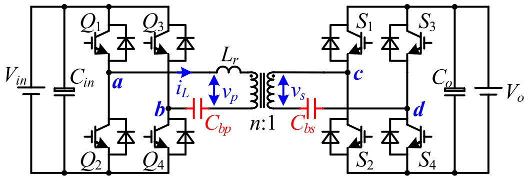

Fig. 1. DAB converter with dc blocking capacitors.

Although these reconfigurable converters can use the simple SPS strategy for efficiency enhancement, the additional switches increase the cost and complicate the topology structure. A simple solution was proposed in [21] and [22], whose main idea is to generate a voltage offset across the dc blocking capacitor, which is placed in series with the isolation transformer, to match the voltage ratio between the two ports. However, in the above publications, the voltage offset in only introduced in the primary side, so the improvement is limited, the converter cannot adapt to wider voltage range and the light-load efficiency does not improve significantly.

In order to improve the efficiency of the DAB, a modified hybrid SPS modulation strategy is proposed to lower the inductor current in this article. The main idea is to introduce a voltage offset across the dc blocking capacitors in both sides, when the voltage ratio varies widely or the transmission power is lower than a certain level. Moreover, the converter can switch between different working modes according to different operating conditions. Then, by regulating only the phase shift angle between the two full bridges, a lower inductor current can be achieved without complicating its implementation. Although a similar idea has been reported in [21] for widening the ZVS range, however, the proposed method could introduce the voltage offsets in both sides, so the converter can adapt to a wider voltage variation and the light-load efficiency enhancement is obvious.

This article is organized as follows. In Section II, the operational principle of four working modes with dc blocking capacitors is introduced. In Section III, the normalized root-mean-square (rms) values of the inductor currents in the four working modes are derived mathematically, which is the foundation of the proposed hybrid modulation. In Section IV, the working mode selection criterion is determined based on the map of inductor current rms value, and the simplified boundaries between different operation modes are proposed for easy implementation. Section V presents the experimental results to verify the performance of the proposed modulation strategy. Finally, Section VI concludes the article and outlines the future work.

II. OPERATIONAL PRINCIPLE BY INTRODUCING DC VOLTAGE OFFSET

A DAB converter consists of two full bridges assembled with switches Q_1–Q_4, S_1–S_4, an isolation transformer with turns ratio of n: 1, an inductor L_r, two dc blocking capacitors C_{bp} and C_{bs}, and two dc bus capacitors C_{in} and C_o, as shown in Fig. 1. Besides, v_{ab} and v_{cd} are pulsed voltages at the alternating terminals of the two full bridges, v_p and v_s are primary and secondary voltages of the transformer, and i_L is the inductor current. Among the components, C_{bp} and C_{bs} may not be necessary with the conventional modulation strategies, if an alternative strategy is adopted to prevent magnetic saturation of the transformer [23]. However, for the proposed modulation strategy, the dc blocking capacitors are necessary.

The conventional SPS scheme for the DAB converter is denoted in Fig. 2(a), where both full bridges are modulated to generate two ac square voltages v_{ab} and v_{cd} with 50% duty cycle each. Since dc offsets of these square voltages are ideally zero, corresponding dc voltage drops across C_{bp} and C_{bs} are also zero. Phase angle between the square voltages can then be regulated to control the power delivered by the converter. With the conventional SPS strategy, the converter is easy to realize ZVS and the reactive power is small when the reflected output voltage nV_o is close to the input voltage V_{in}. However, when the voltage ratio nV_o/V_{in} deviates from 1, the circulating power increases dramatically, which leads to the increased current stress and reduced efficiency.

When the voltage ratio nV_o/V_{in} is smaller than 1, hard switching occurs in the secondary side and reactive power increases, causing efficiency to drop. To rectify, a new modulation strategy for addressing the voltage ratio close to 0.5 is proposed and illustrated in Fig. 2(b), which shows that the gate signals of the new strategy are noticed to be nearly similar to those of conventional SPS. However, the new strategy keeps Q_4 always ON and Q_3 always OFF, instead of pulsewidth modulating them, namely the primary bridge turns into a voltage halver. Then terminal *b* in Fig. 1 is thus clamped to the lower dc rail of the input voltage full bridge and v_{ab} changes from a pure ac voltage to one with a dc component, as shown in Fig. 2(b). Since the duty cycle of v_{ab} is still 50%, the dc component in v_{ab} is simply $V_{\mathrm{in}}/2$.

When the voltage ratio nV_o/V_{in} is larger than 1, hard switching occurs in the primary side and circulating current increases, leading to a lower efficiency. To rectify, a new modulation strategy for addressing the voltage ratio close to 2 is proposed and illustrated in Fig. 2(c), where the gate signals of the new scheme are similar to those of conventional SPS. However, the new scheme keeps S_4 always ON and S_3 always OFF, instead of pulsewidth modulating them, namely the secondary bridge turns into a voltage doubler. Then terminal *d* in Fig. 1 is thus clamped to the lower dc rail of the output voltage full bridge and v_{cd} changes from a pure ac voltage to one with a dc component, as shown in Fig. 2(c). Since the duty cycle of v_{cd} is still 50%, the dc component in v_{cd} is simply $V_o/2$.

In order to improve the efficiency of the DAB converter at light load, a new modulation strategy is proposed and illustrated in Fig. 2(d), where gate signals of the new scheme are similar to those of the conventional SPS strategy. However, the new scheme keeps Q_4/S_4 always ON and Q_3/S_3 always OFF, instead of pulsewidth modulating them, namely the primary bridge turns into a voltage halver and the secondary bridge turns into a voltage doubler. Terminal *b* in Fig. 1 is thus clamped to the lower dc rail of the input full bridge, and terminal *d* is clamped to lower dc rail of the output bridge. Therefore, v_{ab} and v_{cd} change from

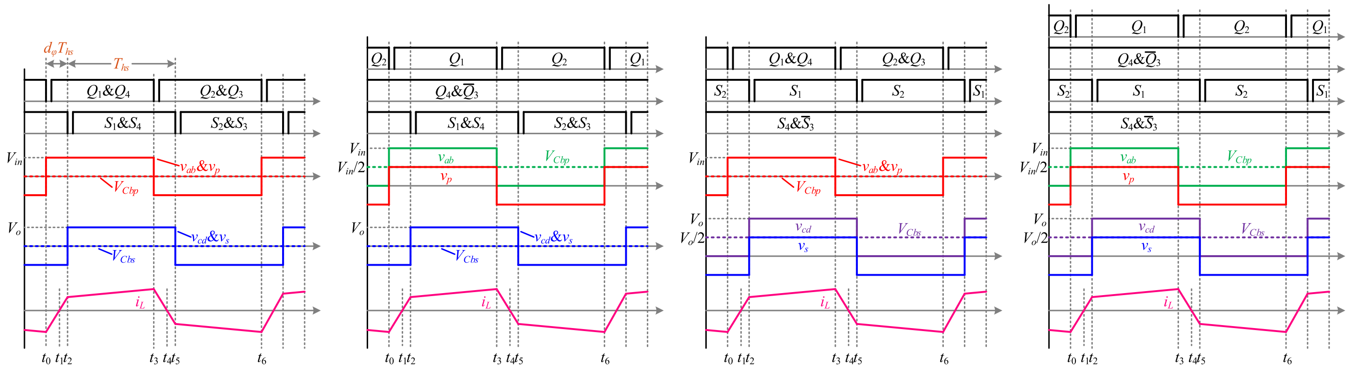

(a) (b) (c) (d)

Fig. 2. Gate signals, voltages, and currents of DAB controlled by (a) conventional SPS scheme, (b) introducing dc offset voltage in the primary side, (c) introducing dc offset voltage in the secondary side, and (d) introducing dc offset voltages in both sides.

a pure ac voltage to one with a dc component, as shown in Fig. 2(d). Since the duty cycle of v_{ab} and v_{cd} are still 50%, the dc components in v_{ab} and v_{cd} are simply $V_{\text{in}}/2$ and $V_o/2$, respectively. For the new modulation strategy in Fig. 2(d), the voltage ratio between the terminal voltages is the same as that of the conventional SPS strategy, but the shifted phase angle should be extended to deliver the same power, which helps to enlarge the soft-switching region and reduce the circulating power, especially at light load.

With the four working modes in Fig. 2, the next key point is how to select the appropriate working mode according to the operating state. In this article, the selection criterion is to lower the rms value of the inductor current; therefore, the current rms value of different modulation schemes will be derived in Section III.

III. INDUCTOR CURRENT RMS VALUE DERIVATION

In this section, the rms value of the inductor current of the four working modes in Fig. 2 will be derived, which is the foundation of the proposed hybrid strategy. For the simplicity of description, the working modes of Fig. 2(a)–(d) are labeled as Mode I: FB/FB, Mode II: HB/FB, Mode III: FB/HB and Mode IV: HB/HB, respectively.

A. Mode I: (FB/FB) Conventional SPS Modulation

The instantaneous currents in Fig. 2(a) can be derived as [24]

$$\begin{cases} i_L(t_0) = \frac{T_{\text{hs}}}{2L_r}\left[(1-2d_\varphi)\,nV_o - V_{\text{in}}\right] \\ i_L(t_2) = \frac{T_{\text{hs}}}{2L_r}\left[nV_o - (1-2d_\varphi)\,V_{\text{in}}\right] \end{cases} \tag{1}$$

where T_{hs} is half of the switching cycle, and d_φ is the phase shift ratio. The transmission power is

$$P = \frac{1}{T_{\text{hs}}}\int_0^{T_{\text{hs}}} v_p(t)\, i_L(t) = \frac{nV_{\text{in}}V_oT_{\text{hs}}}{L_r}(1-d_\varphi)\,d_\varphi \tag{2}$$

when the input and output voltages are matched, namely $V_{\text{in}} = nV_o$, and the shift ratio equals 0.5, the converter can deliver the maximum power, which can be set as the basic power. The expression is as follows:

$$P_{\text{base}} = \frac{V_{\text{in}}V_{\text{in}}T_{\text{hs}}}{L_r}(1-0.5)\,0.5 = \frac{V_{\text{in}}^2T_{\text{hs}}}{4L_r}. \tag{3}$$

Then the normalized power is

$$P^* = \frac{P}{P_{\text{base}}} = 4k\,(1-d_\varphi)\,d_\varphi \tag{4}$$

where k is the ratio between the terminal voltages: $k = nV_o/V_{\text{in}}$.

The basic current can be set in the similar way

$$I_{\text{base}} = \frac{P_{\text{base}}}{V_{\text{in}}} = \frac{V_{\text{in}}T_{\text{hs}}}{4L_r}. \tag{5}$$

Then the normalized currents of (1) can be obtained as

$$\begin{cases} i_L^*(t_0) = \frac{i_L(t_0)}{I_{\text{base}}} = 2\left[(1-2d_\varphi)\,k - 1\right] \\ i_L^*(t_2) = \frac{i_L(t_2)}{I_{\text{base}}} = 2\left[k - (1-2d_\varphi)\right]. \end{cases} \tag{6}$$

Then the rms value of the normalized current can be derived, as expressed in (7), shown at the bottom of the next page.

From (4), the phase shift ratio d_φ can be expressed as

$$d_\varphi = \frac{1-\sqrt{1-P^*/k}}{2}. \tag{8}$$

Substituting (6) and (8) into (7), it is obvious that the normalized rms value is only related to the normalized power P^* and the voltage ratio k. The three-dimensional (3-D) diagram of the normalized current value can be depicted in Fig. 3(a). With the voltage ratio $k = 0.5$, 1, 1.5, and 2, the curves of the current value are illustrated in Fig. 3(b), it can be seen that the curve of $k = 1$ has a lower value in a wide power range, which indicates that the Mode I, namely the traditional SPS, is more suitable for the situation where nV_o equals V_{in}.

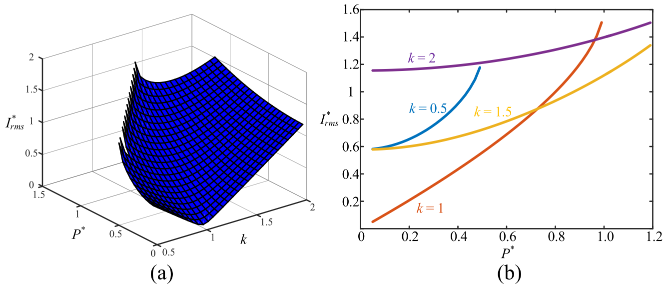

Fig. 3. Normalized rms currents of Mode I (FB/FB). (a) 3-D diagram of rms currents. (b) 2-D curves with $k = 0.5$, 1, 1.5, and 2.

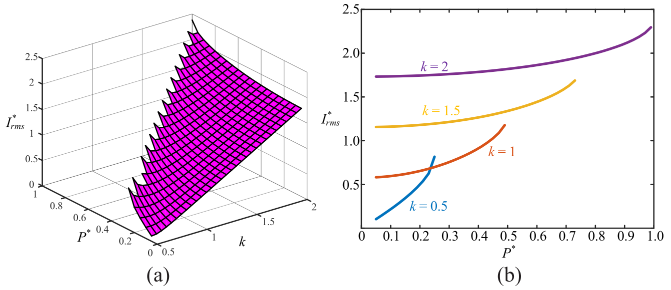

Fig. 4. Normalized rms currents of Mode II (HB/FB). (a) 3-D diagram of rms currents. (b) 2-D curves with $k = 0.5$, 1, 1.5, and 2.

B. *Mode II: (HB/FB) Introducing DC Voltage Offset Across the Primary Blocking Capacitor*

The instantaneous currents in Fig. 2(b) can be derived as

$$\begin{cases} i_L\left(t_0\right) = \frac{T_{\text{hs}}}{2L_r}\left[\left(1-2d_\varphi\right)nV_o - 0.5V_{\text{in}}\right] \\ i_L\left(t_2\right) = \frac{T_{\text{hs}}}{2L_r}\left[nV_o - \left(1-2d_\varphi\right)0.5V_{\text{in}}\right]. \end{cases} \tag{9}$$

Then the normalized currents are

$$\begin{cases} i^*_L\left(t_0\right) = \frac{i_L(t_0)}{I_{\text{base}}} = 2\left[\left(1-2d_\varphi\right)k - 0.5\right] \\ i^*_L\left(t_2\right) = \frac{i_L(t_2)}{I_{\text{base}}} = 2\left[k - 0.5\left(1-2d_\varphi\right)\right]. \end{cases} \tag{10}$$

The transmission power is

$$P = \frac{1}{T_{\text{hs}}}\int_0^{T_{\text{hs}}} v_p\left(t\right)i_L\left(t\right) = \frac{0.5V_{\text{in}}nV_oT_{\text{hs}}}{L_r}\left(1-d_\varphi\right)d_\varphi. \tag{11}$$

Then the normalized power is

$$P^* = \frac{P}{P_{\text{base}}} = 2k\left(1-d_\varphi\right)d_\varphi. \tag{12}$$

The phase shift ratio d_φ is

$$d_\varphi = \frac{1-\sqrt{1-2P^*/k}}{2}. \tag{13}$$

The rms value of the normalized current can be derived in the same way as (7)

$$I^*_{\text{rms}} = \sqrt{\begin{array}{l}\int_0^{d_\varphi}\left[i^*_L\left(t_0\right)+4\left(0.5+k\right)x\right]^2dx \\ +\int_{d_\varphi}^1\left[i^*_L\left(t_2\right)+4\left(0.5-k\right)\left(x-d_\varphi\right)\right]^2dx\end{array}}. \tag{14}$$

The 3-D diagram of the normalized current value can be depicted in Fig. 4(a). With the voltage ratio $k = 0.5$, 1, 1.5, and 2, the curves of the current value are illustrated in Fig. 4(b), it can be seen that the curve of $k = 0.5$ has a lower value in almost the whole power range, which indicates that the Mode II (HB/FB) strategy is more suitable for the situation of $k = 0.5$, namely nV_o is half of V_{in}.

C. *Mode III: (FB/HB) Introducing DC Voltage Offset Across the Secondary Blocking Capacitor*

The instantaneous currents in Fig. 2(c) can be derived as

$$\begin{cases} i_L\left(t_0\right) = \frac{T_{\text{hs}}}{2L_r}\left[\left(1-2d_\varphi\right)0.5nV_o - V_{\text{in}}\right] \\ i_L\left(t_2\right) = \frac{T_{\text{hs}}}{2L_r}\left[0.5nV_o - \left(1-2d_\varphi\right)V_{\text{in}}\right]. \end{cases} \tag{15}$$

Then the normalized currents are obtained as

$$\begin{cases} i^*_L\left(t_0\right) = \frac{i_L(t_0)}{I_{\text{base}}} = 2\left[\left(1-2d_\varphi\right)0.5k - 1\right] \\ i^*_L\left(t_2\right) = \frac{i_L(t_2)}{I_{\text{base}}} = 2\left[0.5k - \left(1-2d_\varphi\right)\right]. \end{cases} \tag{16}$$

The transmission power is

$$P = \frac{1}{T_{\text{hs}}}\int_0^{T_{\text{hs}}} v_p\left(t\right)i_L\left(t\right) = \frac{V_{\text{in}}0.5nV_oT_{\text{hs}}}{L_r}\left(1-d_\varphi\right)d_\varphi. \tag{17}$$

Then the normalized power is

$$P^* = \frac{P}{P_{\text{base}}} = 2k\left(1-d_\varphi\right)d_\varphi. \tag{18}$$

$$\begin{aligned} I^*_{\text{rms}} &= \frac{\sqrt{\frac{\int_0^{d_\varphi T_{\text{hs}}}\left[i_L(t_0)+\frac{V_{\text{in}}+nV_o}{L_r}t\right]^2dt+\int_{d_\varphi T_{\text{hs}}}^{T_{\text{hs}}}\left[i_L(t_2)+\frac{V_{\text{in}}-nV_o}{L_r}(t-d_\varphi T_{\text{hs}})\right]^2dt}{T_{\text{hs}}}}}{I_{\text{base}}} \\ &= \sqrt{\frac{\int_0^{d_\varphi T_{\text{hs}}}\left[i^*_L\left(t_0\right)+4\left(1+k\right)\frac{t}{T_{\text{hs}}}\right]^2dt+\int_{d_\varphi T_{\text{hs}}}^{T_{\text{hs}}}\left[i^*_L\left(t_2\right)+4\left(1-k\right)\left(\frac{t}{T_{\text{hs}}}-d_\varphi\right)\right]^2dt}{T_{hs}}} \\ &\qquad\qquad \Updownarrow \quad (\text{suppose } x = t/T_{\text{hs}}) \\ &= \sqrt{\int_0^{d_\varphi}\left[i^*_L\left(t_0\right)+4\left(1+k\right)x\right]^2dx+\int_{d_\varphi}^1\left[i^*_L\left(t_2\right)+4\left(1-k\right)\left(x-d_\varphi\right)\right]^2dx} \end{aligned} \tag{7}$$

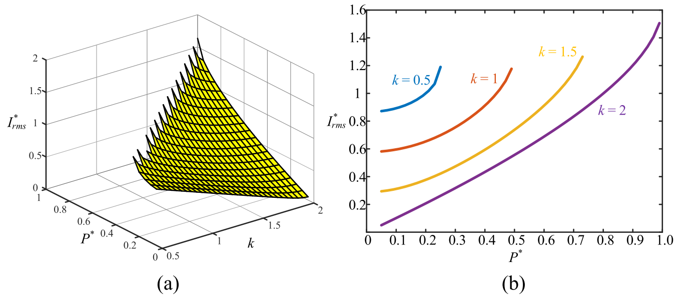

Fig. 5. Normalized rms currents of Mode III (FB/HB). (a) 3-D diagram of rms currents. (b) 2-D curves with $k = 0.5$, 1, 1.5, and 2.

The phase shift ratio d_φ can be obtained as

$$d_\varphi = \frac{1-\sqrt{1-2P^*/k}}{2}. \tag{19}$$

The rms value of the normalized current can be derived in the same way as (7)

$$I^*_{\mathrm{rms}} = \sqrt{\begin{array}{l}\int_0^{d_\varphi}\left[i^*_L\left(t_0\right)+4\left(1+0.5k\right)x\right]^2dx\\ +\int_{d_\varphi}^1\left[i^*_L\left(t_2\right)+4\left(1-0.5k\right)\left(x-d_\varphi\right)\right]^2dx\end{array}}. \tag{20}$$

The 3-D diagram of the normalized current value can be depicted in Fig. 5(a). With the voltage ratio $k = 0.5$, 1, 1.5, and 2, the curves of the current value are illustrated in Fig. 5(b), it can be seen that the curve of $k = 2$ has a lower value in the entire power range, which indicates that the Mode III (FB/HB) strategy is more suitable for the situation of $k = 2$, namely V_{in} is half of nV_o.

D. Mode IV: (HB/HB) Introducing DC Voltage Offsets in Both Sides

The instantaneous currents in Fig. 2(d) can be derived as

$$\begin{cases} i_L\left(t_0\right) = \frac{T_{\mathrm{hs}}}{2L_r}\left[\left(1-2d_\varphi\right)0.5nV_o - 0.5V_{\mathrm{in}}\right] \\ i_L\left(t_2\right) = \frac{T_{\mathrm{hs}}}{2L_r}\left[0.5nV_o - \left(1-2d_\varphi\right)0.5V_{\mathrm{in}}\right]. \end{cases} \tag{21}$$

Then the normalized currents are obtained as

$$\begin{cases} i^*_L\left(t_0\right) = \frac{i_L(t_0)}{I_{\mathrm{base}}} = 2\left[\left(1-2d_\varphi\right)0.5k - 0.5\right] \\ i^*_L\left(t_2\right) = \frac{i_L(t_2)}{I_{\mathrm{base}}} = 2\left[0.5k - 0.5\left(1-2d_\varphi\right)\right]. \end{cases} \tag{22}$$

The transmission power is

$$P = \frac{1}{T_{\mathrm{hs}}}\int_0^{T_{\mathrm{hs}}} v_p\left(t\right)i_L\left(t\right) = \frac{0.5V_{\mathrm{in}}0.5nV_oT_{hs}}{L_r}\left(1-d_\varphi\right)d_\varphi. \tag{23}$$

Then the normalized power is

$$P^* = \frac{P}{P_{\mathrm{base}}} = k\left(1-d_\varphi\right)d_\varphi. \tag{24}$$

The phase shift ratio d_φ can be obtained as

$$d_\varphi = \frac{1-\sqrt{1-4P^*/k}}{2}. \tag{25}$$

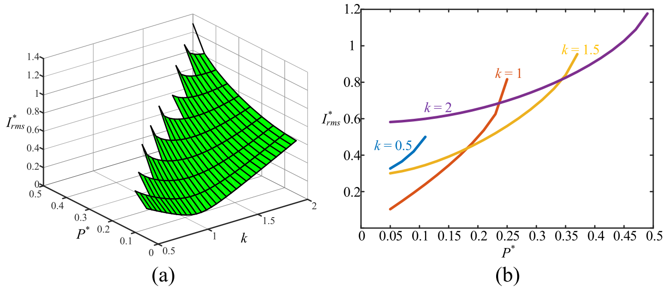

Fig. 6. Normalized rms currents of Mode IV (HB/HB). (a) 3-D diagram of rms currents. (b) 2-D curves with $k = 0.5$, 1, 1.5, and 2.

The rms value of the normalized current can be derived in the same way as (7)

$$I^*_{\mathrm{rms}} = \sqrt{\begin{array}{l}\int_0^{d_\varphi}\left[i^*_L\left(t_0\right)+2\left(1+k\right)x\right]^2dx\\ +\int_{d_\varphi}^1\left[i^*_L\left(t_2\right)+2\left(1-k\right)\left(x-d_\varphi\right)\right]^2dx\end{array}}. \tag{26}$$

The 3-D diagram of the normalized current value can be depicted in Fig. 6(a), which shows that the transmission power capability has been reduced significantly compared to Fig. 3(a). With the voltage ratio $k = 0.5$, 1, 1.5, and 2, the curves of the current value are illustrated in Fig. 6(b), it can be seen that the curves of the same voltage ratio k has a lower current value than that in Fig. 3(b) when delivering the same power, especially at light load.

IV. Hybrid Modulation Strategy

From the analysis above, it can be observed that different working modes are suitable for different operating conditions. If the best working modes are selected for the specific operating condition, then the lowest current value can be achieved through the entire operating regions.

When the voltage ratio k is fixed, the graphs of normalized rms currents with different working modes are shown in Fig. 7. Take the Fig. 7(a) as an example, if the converter can operate in Mode II (HB/FB) when the transmission power P^* is less than 0.25, and operate in Mode I (FB/FB) when P^* is larger than 0.25, the rms current value can maintain the minimum value through the entire range of transmission power. So the next key point is to find the critical boundary conditions between different working modes to make the converter operate in the optimal status.

A. Derivation of the Boundaries Conditions

Integrating the 3-D diagrams of the normalized rms current in the four operation modes, namely Figs. 3(a), 4(a), 5(a), and 6(a), into a diagram, as shown in Fig. 8(a), which shows clearly that if different modulation strategies can be selected according to the operating point, then a lower inductor current can be obtained. So it is necessary to propose a hybrid modulation strategy, of which the key point is how to determine the operation regions of different modulation strategies.

The bottom view of Fig. 8(a) is illustrated in Fig. 8(b), which shows that when the voltage ratio k is less than 0.6, the Mode II

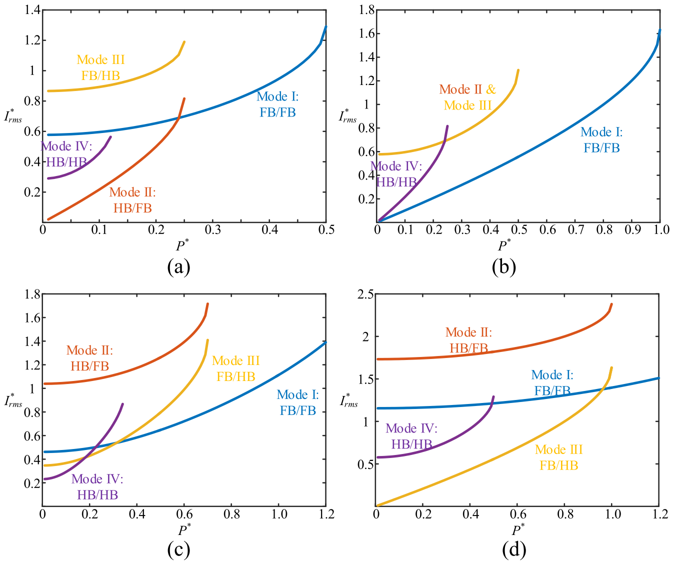

(a) (b) (c) (d)

Fig. 7. Normalized rms currents with different woking modes: (a) $k = 0.5$, (b) $k = 1$, (c) $k = 1.4$, and (d) $k = 2$.

TABLE I
EXPRESSION OF THE SIMPLIFIED BOUNDARY LINES

Boundaries	Expression
a	$P^* = 0.478k$
b	$P^* = -0.063k + 0.261$
c	$P^* = -1.375k + 1.114$
d	$P^* = 1.667k - 1.107$
e	$P^* = -0.417k + 0.414$
f	$P^* = 0.559k - 0.56$
g	$P^* = -0.778k + 1.258$
h	$P^* = -2.4k + 3.61$
i	$P^* = 2k - 2.52$
j	$P^* = 1.095k - 1.153$
k	$P^* = 0.821k - 0.682$

(HB/FB) can achieve the lowest rms current value for the light load; when the voltage ratio k is larger than 1.5, the Mode III (FB/HB) can achieve the lowest rms current value in a large transmission power range; when the voltage ratio k is around 1 and the transmission power is very low, the Mode IV (HB/HB) is the best choice for rms current value reduction.

If the converter can work in different operation mode according to Fig. 8(b), then the lowest rms current value can be guaranteed for a wide voltage range and a wide load range. The boundaries in Fig. 8(b) can be obtained by solving the equations of (7), (14), (20), and (26). However, the calculation is complicated and the obtained results could lead to a heavy computation burden for implementation in the microprocessor.

In order to simplify the expressions of the boundaries and reduce the computation burden, a bunch of linear lines is used to approximate the original boundaries, as shown the dot lines from a to k in Fig. 8(b).

The expressions of the simplified boundary lines in Fig. 8(b) are listed in Table I.

With the simplified boundaries, the operation region of Mode II (HB/FB) can be defined by the lines of a, b, c, and d, shown as follows:

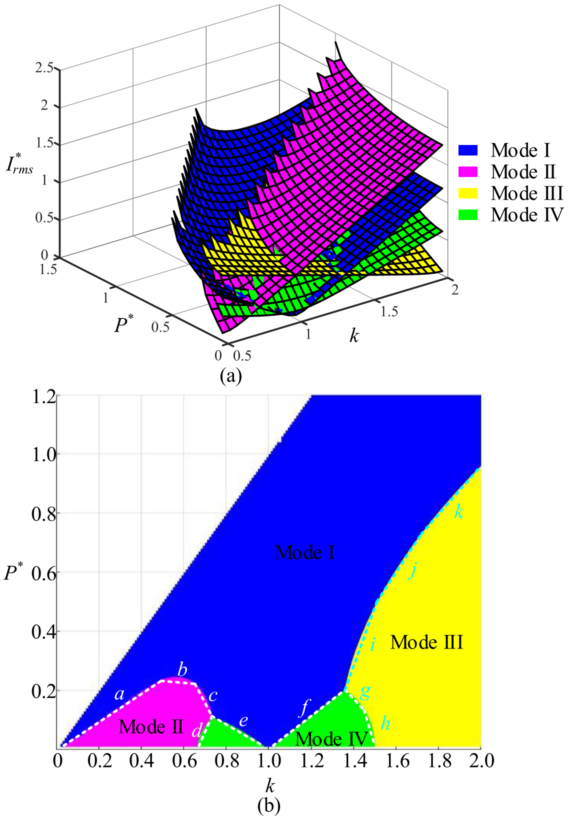

(a)

(b)

Fig. 8. (a) 3-D diagram of the normalized rms current value in different operation modes. (b) Bottom view of the 3-D diagram and simplified boundaries.

$$\begin{cases} (P^* < 0.478k)\ \&\& \\ (P^* < -0.063k + 0.261)\ \&\& \\ (P^* < -1.375k + 1.114)\ \&\& \\ (P^* > 1.667k - 1.107)\,. \end{cases} \tag{27}$$

The operation region of Mode III (FB/HB) can be defined by the lines of g, h, i, j, and k, shown as follows:

$$\begin{cases} \left(\begin{array}{l} (P^* > -0.778k + 1.258)\ \| \\ (P^* > -2.4k + 3.61) \end{array} \right) \&\& \\ (P^* < 2k - 2.52)\ \&\& \\ (P^* < 1.095k - 1.153)\ \&\& \\ (P^* < 0.821k - 0.682)\,. \end{cases} \tag{28}$$

The operation region of Mode IV (HB/HB) can be defined by the lines of d, e, f, g, and h, given as follows:

$$\begin{cases} \left(\begin{array}{l} (P^* < 1.667k - 1.107)\ \&\& \\ (P^* < -0.417k + 0.414) \end{array} \right) \| \\ \left(\begin{array}{l} (P^* < 0.559k - 0.56)\ \&\& \\ (P^* < -0.778k + 1.258)\ \&\& \\ (P^* < -2.4k + 3.61) \end{array} \right) \end{cases} . \tag{29}$$

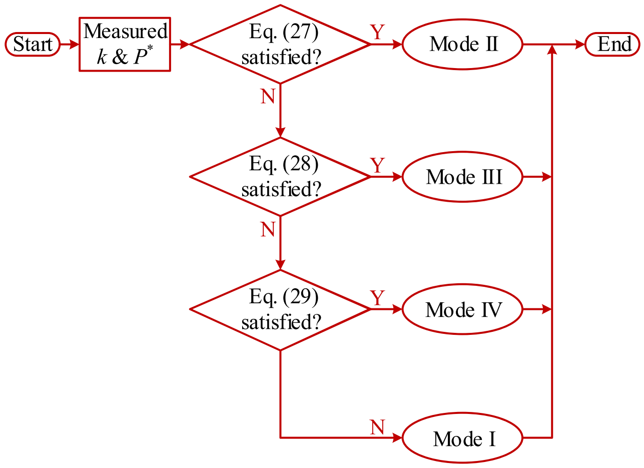

Fig. 9. Diagram of switching modes.

With these simplified expressions of boundaries, the divided operating regions can be redrawn as Fig. 8(b). It can be seen that the differences between the regions determined by the original boundaries and the simplified boundaries are relatively small, which is good for the implementation in practice.

According to Table I and the simplified divided regions of Fig. 8(b), a hybrid modulation strategy can be obtained, and the mode switching diagram is illustrated in Fig. 9.

Another key point of the proposed hybrid modulation strategy is how to switch from one working mode to another. This issue was explained in detail in [21], so it will not be repeated here.

B. Discussion of the ZVS Regions

The ZVS regions of different working modes will be presented in this part, take the Mode I (FB/FB) as an example, the derivation process is as follows:

In Mode I (FB/FB), the soft condition for the primary switches is

$$\begin{cases} i_L\left(t_0\right) < 0 \\ \frac{1}{2}L_r i_L^2\left(t_0\right) > 4\frac{1}{2}C_p V_{\text{in}}^2 \end{cases} \tag{30}$$

where C_p is the junction capacitor of the primary switch. Equation (30) can be simplified as

$$i_L\left(t_0\right) < -2V_{\text{in}}\sqrt{\frac{C_p}{L_r}}. \tag{31}$$

Substituting (1) into (31), it can be obtained as

$$d_\varphi > \frac{k-1}{2k} + \frac{2}{kT_{hs}}\sqrt{L_r C_p}. \tag{32}$$

On the other hand, the soft-switching condition for the secondary switches is

$$\begin{cases} i_L\left(t_2\right) > 0 \\ \frac{1}{2}L_r i_L^2\left(t_2\right) > 4\frac{1}{2}C_s V_o^2 \end{cases} \tag{33}$$

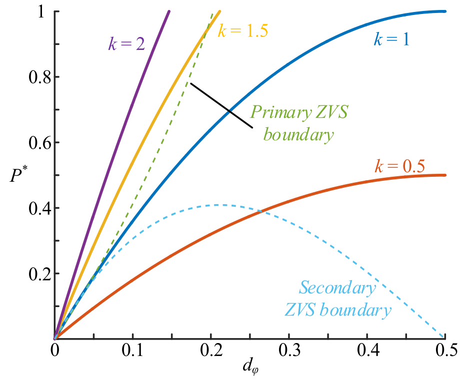

Fig. 10. Curves of transmission power and ZVS boundaries.

where C_s is the junction capacitor of the secondary switch. Substituting (1) into (33), it can be obtained as

$$d_\varphi > \frac{1-k}{2} + \frac{2k}{nT_{\text{hs}}}\sqrt{L_r C_s}. \tag{34}$$

Substituting the normalized power expression (4) into (32) and (34), the ZVS boundary corresponding to the phase shift factor d_φ can be obtained as

$$\begin{cases} P^* < \frac{4d_\varphi(1-d_\varphi)\left(1-\frac{4}{T_{\text{hs}}}\sqrt{L_r C_p}\right)}{1-2d_\varphi} \\ P^* > \frac{4d_\varphi(1-d_\varphi)(1-2d_\varphi)}{1-\frac{4}{nT_{\text{hs}}}\sqrt{L_r C_s}}. \end{cases} \tag{35}$$

The ZVS boundary of (35) and the transmission curves with $k = 0.5$, 1, 1.5, 2 are depicted in Fig. 10, which shows that the converter can realize ZVS almost in the entire load range as the voltage ratio k equals 1; however, the primary switches are not able to realize ZVS at light load when k is larger than 1 and the secondary switches are hard to achieve ZVS at light load when k is less than 1.

Substituting (32) and (34) into (4), the ZVS boundary corresponding to the voltage ratio k can be obtained as

$$\begin{cases} P^* > 4k\left(\frac{k-1}{2k} + \frac{2}{kT_{\text{hs}}}\sqrt{L_r C_p}\right)\left(1 - \frac{k-1}{2k} - \frac{2}{kT_{\text{hs}}}\sqrt{L_r C_p}\right) \\ P^* > 4k\left(\frac{1-k}{2} + \frac{2k}{nT_{\text{hs}}}\sqrt{L_r C_s}\right)\left(1 - \frac{1-k}{2} - \frac{2k}{nT_{\text{hs}}}\sqrt{L_r C_s}\right). \end{cases} \tag{36}$$

The ZVS boundaries of (36) and the maximum transmission power line are depicted in Fig. 11(a). Based on the same principle, the ZVS regions of Mode II (FB/HB), Mode III (HB/FB), and Mode IV (HB/HB) can also be derived and illustrated in Fig. 11(b)–(d), respectively.

Compared with the region of the lowest rms current value, as shown in Fig. 8(b), it can be observed that most operating regions in Fig. 8(b) overlap with the ZVS regions in Fig. 11, which indicates that the proposed method realizes both the ZVS and the lowest current value in these operating regions.

Indeed, in a small part of the operating regions, especially the area around the boundary, the ZVS and the lowest current value cannot be satisfied at the same time. In this article, the lowest current rms value is the optimization goal, so the proposed method pursues the smaller conduction losses instead of the

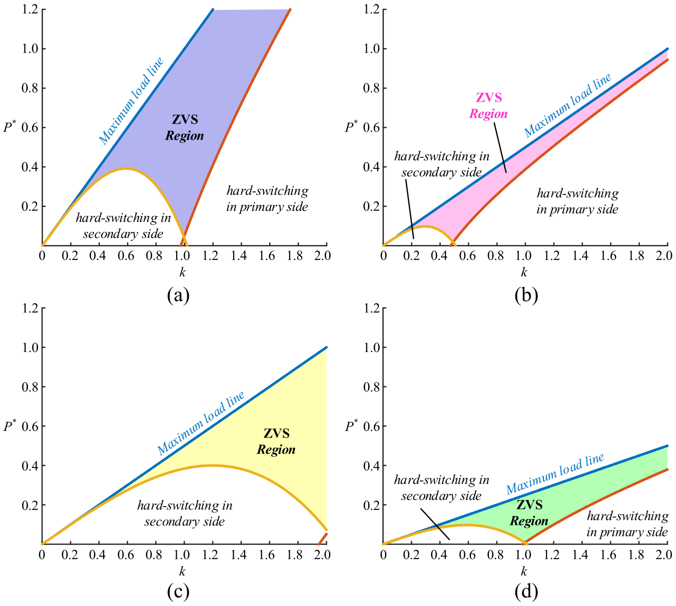

(a) (b) (c) (d)

Fig. 11. ZVS regions of different working modes. (a) Mode I: FB/FB. (b) Mode II: HB/FB. (c) Mode III: FB/HB. (d) Mode IV: HB/HB.

TABLE II
PARAMETERS OF THE PROTOTYPE

Components	Parameters
Input voltage (V_{in})	100-350 V
Output voltage (V_o)	360 V
Nominal power (P_n)	6 kW
Switching frequency (f_s)	50 kHz
Turns ratio of transformer (n)	8: 13
Transfer inductor (L_r)	17 μH
Input capacitor (C_{in})	4080 μF
Output capacitor (C_o)	4080 μF
Primary switches (Q_1-$Q4$)	2×IXFK80N50P
Secondary switches (S_1-S_4)	IXFK80N50P
Blocking capacitor C_{bp}	28.6 μF (13×CBB 225 J)
Blocking capacitor C_{bs}	17.6 μF (8×CBB 225 J)

switching losses. However, it should be noted that the boundary conditions between different working modes can be adjusted for different purposes in different applications, so the proposed method can be extended to other forms to achieve other goals.

V. EXPERIMENTAL VERIFICATION

In this section, the experimental results are presented to verify the performance of the proposed modulation strategy. In the laboratory, a 6-kW power prototype is built for the experimental test, whose specification and parameters are listed in Table II, and the photo is shown in Fig. 12, where the magnetic devices and the dc blocking capacitors are located under the power boards. The selection principle of the dc blocking capacitor is to ensure the voltage ripple across the capacitor is less than a certain value [21], so that it will not have a negative impact on the operation of the converter. In addition, since the capacitor has to pass the whole transfer current, it is necessary to select the capacitor with an appropriate rated current.

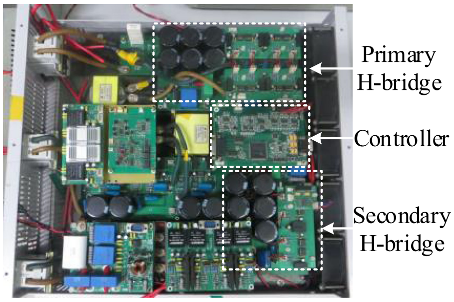

Fig. 12. Photo of the experimental prototype.

A. Experimental Waveforms

First, different operating points of different sections in Fig. 8 are selected to compare the inductor current values in different working modes.

When the input voltage V_{in} is 340 V and the transmission power P is 1.71kW, the experimental waveforms of the operating point $(k, P^*) = (0.65, 0.1)$ under different operation modes are shown in Fig. 13, which shows clearly that Mode II (HB/FB) has the lowest current value. According to Fig. 9, the operating point $(k, P^*) = (0.65, 0.1)$ satisfies the condition of (27), then the Mode II strategy is adopted, thus the hybrid modulation can achieve the lowest current value.

When the input voltage V_{in} is 295 V and the transmission power P is 641 W, the experimental waveforms of the operating point $(k, P^*) = (0.75, 0.05)$ under different operation modes are shown in Fig. 14, which shows clearly that Mode IV (HB/HB) has the lowest current value. According to Fig. 9, the operating point $(k, P^*) = (0.75, 0.05)$ satisfies the condition of (29), then the Mode IV strategy is adopted, thus the hybrid modulation can achieve the lowest current value.

When the input voltage V_{in} is 221 V and the transmission power P is 1.44 kW, the experimental waveforms of the operating point $(k, P^*) = (1, 0.2)$ under different operation modes are shown in Fig. 15, which shows clearly that Mode I (FB/FB) has the lowest current value. According to Fig. 9, the operating point $(k, P^*) = (1, 0.2)$ does not satisfy the conditions of (27)–(29), then the Mode I strategy is adopted, thus the hybrid modulation can achieve the lowest current value.

When the input voltage V_{in} is 158 V and the transmission power P is 368W, the experimental waveforms of the operating point $(k, P^*) = (1.4, 0.1)$ under different operation modes are shown in Fig. 16, which shows clearly that Mode IV (HB/HB) has the lowest current value. According to Fig. 9, the operating point $(k, P^*) = (1.4, 0.1)$ satisfies the condition of (29), then the Mode IV strategy is adopted, thus the hybrid modulation can achieve the lowest current value.

When the input voltage V_{in} is 111 V and the transmission power P is 722 W, the experimental waveforms of the operating point $(k, P^*) = (2, 0.4)$ under different operation modes are shown in Fig. 17, which shows clearly that Mode III (FB/HB)

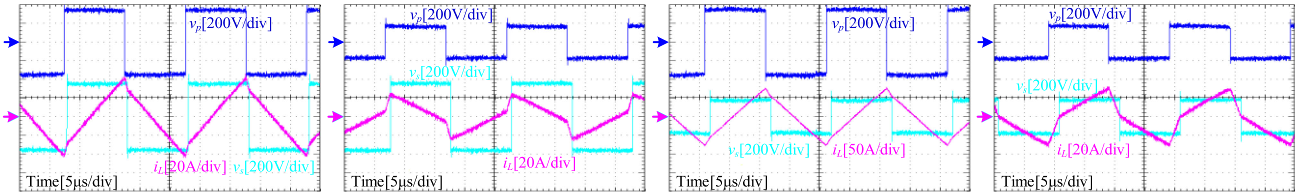

(a) (b) (c) (d)

Fig. 13. When $V_{\text{in}} = 340$ V, $V_o = 360$ V, and $P = 1.71$ kW, experimental waveforms of (0.65, 0.1). (a) Mode I. (b) Mode II. (c) Mode III. (d) Mode IV.

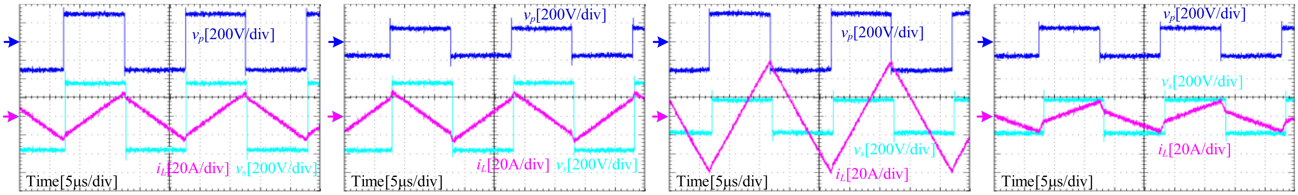

(a) (b) (c) (d)

Fig. 14. When $V_{\text{in}} = 295$ V, $V_o = 360$ V, and $P = 641$W, experimental waveforms of (0.75, 0.05). (a) Mode I, (b) Mode II, (c) Mode III, and (d) Mode IV.

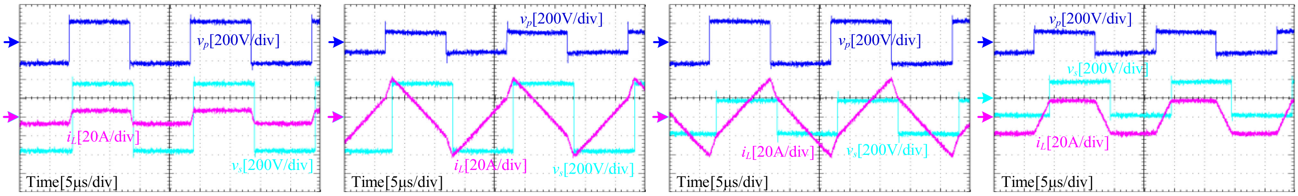

(a) (b) (c) (d)

Fig. 15. When $V_{\text{in}} = 221$ V, $V_o = 360$ V, and $P = 1.44$ kW, experimental waveforms of (1, 0.2). (a) Mode I. (b) Mode II. (c) Mode III. (d) Mode IV.

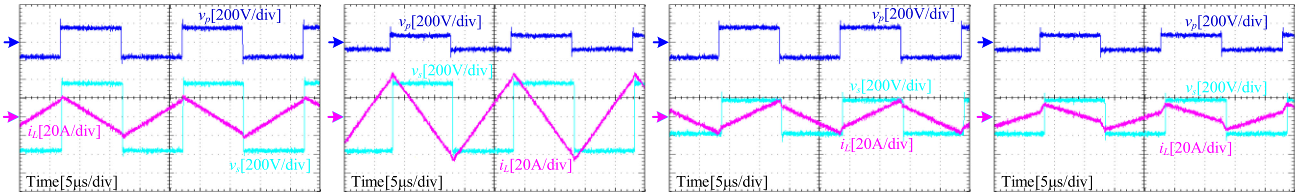

(a) (b) (c) (d)

Fig. 16. When $V_{\text{in}} = 158$ V, $V_o = 360$ V, $P = 368$ W, experimental waveforms of (1.4, 0.1). (a) Mode I. (b) Mode II. (c) Mode III. (d) Mode IV.

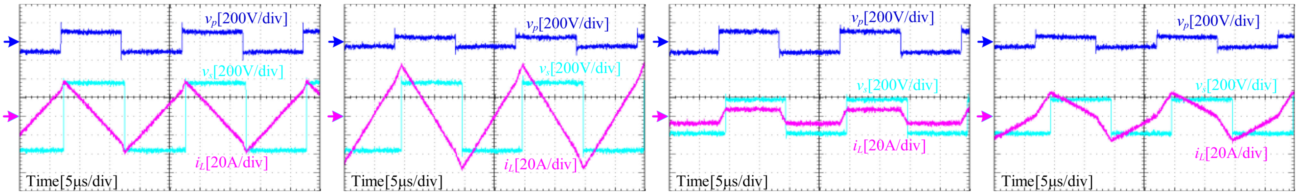

(a) (b) (c) (d)

Fig. 17. When $V_{\text{in}} = 111$ V, $V_o = 360$ V, $P = 722$ kW, experimental waveforms of (2, 0.4). (a) Mode I. (b) Mode II. (c) Mode III. (d) Mode IV.

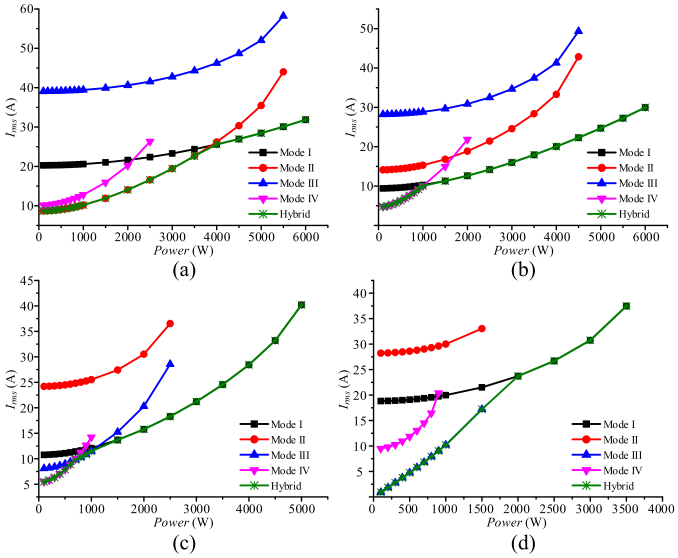

Fig. 18. RMS current value comparison between different working modes. (a) $V_{\text{in}} = 340$ V, $V_o = 360$ V, $k = 0.65$. (b) $V_{\text{in}} = 277$ V, $V_o = 360$ V, $k = 0.8$. (c) $V_{\text{in}} = 158$ V, $V_o = 360$ V, $k = 1.4$. (d) $V_{\text{in}} = 111$ V, $V_o = 360$ V, $k = 2$.

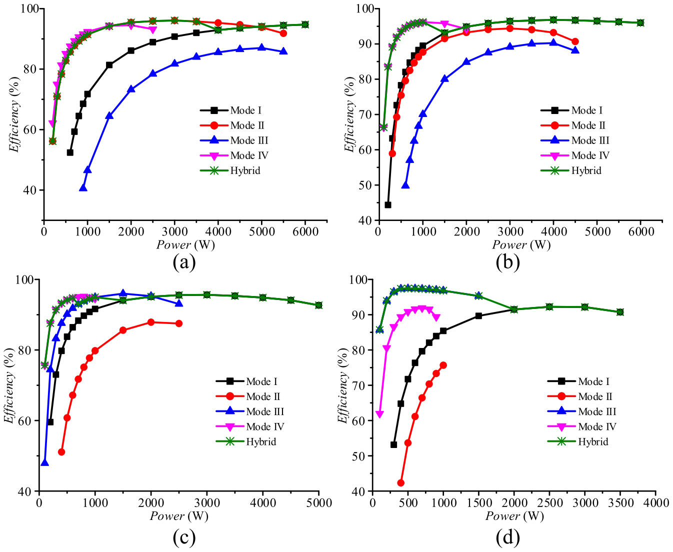

Fig. 19. Efficiency comparison between different working modes, (a) $V_{\text{in}} = 340$ V, $V_o = 360$ V, $k = 0.65$. (b) $V_{\text{in}} = 277$ V, $V_o = 360$ V, $k = 0.8$. (c) $V_{\text{in}} = 158$ V, $V_o = 360$ V, $k = 1.4$. (d) $V_{\text{in}} = 111$ V, $V_o = 360$ V, $k = 2$.

has the lowest current value. According to Fig. 9, the operating point (k, P^*) = (2, 0.4) satisfies the condition of (28), then the Mode III strategy is adopted, thus the hybrid modulation can achieve the lowest current value.

B. Inductor Current Comparison

Fig. 18(a)–(d) show the inductor current rms value comparison between different operation modes with the voltage ratio $k = 0.65$, 0.8, 1.4, and 2, respectively.

When k equals 0.65, it can be observed from Fig. 18(a) that the rms value curve of the hybrid modulation tracks Mode II when the transmission power is lower than 4 kW; on the other hand, it tracks Mode I when the power is higher than 4 kW. So the proposed hybrid modulation can achieve the lowest inductor current value over the entire power range.

Fig. 18(b)–(d) can be analyzed in the same way, the proposed hybrid modulation always tracks the lowest inductor current value in the whole transmission power range with different voltage ratios.

C. Efficiency Comparison

Fig. 19(a)–(d) shows the efficiency comparison between different operation modes with the voltage ratio $k = 0.65$, 0.8, 1.4, and 2, respectively.

When k equals 0.65, it can be observed from Fig. 19(a) that the efficiency curve of the hybrid modulation tracks Mode II when the transmission power is lower than 4 kW; on the other hand, it tracks Mode I when the power is higher than 4 kW. So the proposed hybrid modulation operates at the optimal efficiency point almost in the entire power range. Fig. 19(b)–(d) can be analyzed in the same way, the proposed hybrid modulation tracks the best efficiency point almost in the whole transmission power range.

It can also be noticed that at some operating points, the hybrid modulation does not adopt the best modulation, such as the point of 4000 W in Fig. 19(a), the point of 1500 W in Fig. 19(b) and the point of 1500 W in Fig. 19(c). The error mainly comes from this aspect: the selection criterion for different working modes is to lower the inductor current, so the conduction loss of the switches and the loss of the magnetic devices can be reduced, however, the switching loss is not taken into account. When the conduction loss is minimum, which does not mean the total loss is minimum, so the proposed modulation does not reach the best efficiency at some operating points. It should be emphasized that the errors only occur in a very narrow power range; moreover, the efficiency decay is not drastic, so it is acceptable for a simple and practical solution.

The idea of introducing dc blocking capacitors was proposed in [21]; however, the method in [21] is very simple. The boundary between different working modes is $k = 1.2$: when the voltage ratio k is less than 1.2, and the converter operates in Mode I (FB/FB); when the voltage ratio k is larger than 1.2, the converter operates in Mode III (FB/HB). It can be observed from Fig. 19 that the proposed method has obvious advantages over the method in [21] due to that the proposed hybrid modulation has more working modes and the boundary conditions are more accurate.

The proposed hybrid method has also been compared with the advanced TPS modulation, which focuses on efficiency optimization [14]. The comparison results are shown in Fig. 20.

When the voltage ratio $k = 1$, namely the terminal voltages are matched, the efficiency performance of the two methods is almost the same; when the voltage ratio $k = 0.65$ or $k = 1.4$, each method has the advantage over the other method in part of the transmission power range. The proposed method needs dc blocking capacitors, and only needs a simple on-line working mode identification algorithm to switch between different

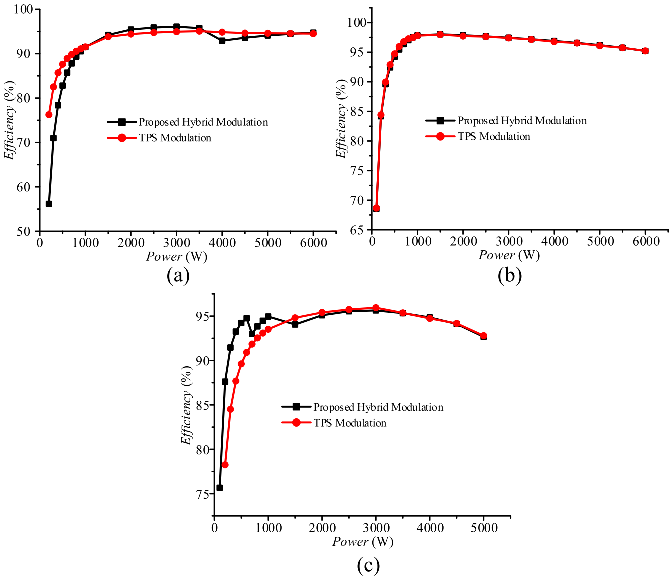

(a) (b) (c)

Fig. 20. Efficiency comparison between the proposed method and the TPS modulation. (a) $V_{\text{in}} = 340$ V, $V_o = 360$ V, $k = 0.65$. (b) $V_{\text{in}} = 221$ V, $V_o = 360$ V, $k = 1$. (c) $V_{\text{in}} = 158$, $V_o = 360$ V, $k = 1.4$

working modes. For the TPS modulation, it does not need extra devices, but the optimized algorithms are very complicated to implement. The two methods both have their advantages and disadvantages, and they can be chosen according to the practical applications.

VI. CONCLUSION

With the conventional SPS modulation strategy, the DAB converter will generate a large amount of circulating power when the voltage varies widely, resulting in the increased current stress and reduced efficiency. In order to improve the performance of the DAB converter over wide voltage range and wide load range, a hybrid modulation strategy was proposed in this article, whose core idea was to introduce a voltage offset across the dc blocking capacitors in both sides, and the converter could switch between different operating modes to lower the inductor current. The proposed hybrid modulation technique retained the simplicity of SPS strategy and did not complicate the topology structure. The performance was verified by the experimental results: the hybrid modulation achieved the lowest inductor current value and tracked the operating points of the best efficiency almost in the entire load range with different voltage ratios.

REFERENCES

[1] R. D. Doncker, D. M. Divan, and M. H. Kheraluwala, “A three-phase soft-switched high-power-density dc/dc converter for high-power applications,” *IEEE Trans. Ind. Appl.*, vol. 27, no. 1, pp. 63–73, Jan. 1991.

[2] N. H. Baars, J. Everts, C. G. E. Wijnands, and E. A. Lomonova, “Performance evaluation of a three-phase dual active bridge DC–DC converter with different transformer winding configurations,” *IEEE Trans. Power Electron.*, vol. 31, no. 10, pp. 6814–6823, Oct. 2016.

[3] Y. Shi, R. Li, Y. Xue, and H. Li, “Optimized operation of current-fed dual active bridge DC–DC converter for PV applications,” *IEEE Trans. Ind. Electron.*, vol. 62, no. 11, pp. 6986–6995, Nov. 2015.

[4] P. Liu, C. Chen, S. Duan, and W. Zhu, “Dual phase-shifted modulation strategy for the three-level dual active bridge DC–DC converter,” *IEEE Trans. Ind. Electron.*, vol. 64, no. 10, pp. 7819–7830, Oct. 2017.

[5] P. Liu, C. Chen, and S. Duan, “An optimized modulation strategy for the three-level DAB converter with five control degrees of freedom,” *IEEE Trans. Ind. Electron.*, to be published, doi: 10.1109/TIE.2019.2896209.

[6] B. Zhao, Q. Song, W. Liu, and Y. Xiao, “Next-generation multi-functional modular intelligent UPS system for smart grid,” *IEEE Trans. Ind. Electron.*, vol. 60, no. 9, pp. 3602–3618, Sep. 2013.

[7] B. Zhao, Q. Song, and W. Liu, “A practical solution of high-frequency-link bidirectional solid-state transformer based on advanced components in hybrid microgrid,” *IEEE Trans. Ind. Electron.*, vol. 62, no. 7, pp. 4587–4597, Jul. 2015.

[8] X. She, A. Q. Huang, and R. Burgos, “Review of solid-state transformer technologies and their application in power distribution systems,” *IEEE J. Emerg. Sel. Topics Power Electron.*, vol. 1, no. 3, pp. 186–198, Sep. 2013.

[9] Z. Liu, B. Li, F. C. Lee, and Q. Li, “High-efficiency high-density critical mode rectifier/inverter for wbg-device-based on-board charger,” *IEEE Trans. Ind. Electron.*, vol. 64, no. 11, pp. 9114–9123, Nov. 2017.

[10] B. Zhao, Q. Song, J. Li, Y. Wang, and W. Liu, “Modular multilevel high-frequency-link DC transformer based on dual active phase-shift principle for medium-voltage DC power distribution application,” *IEEE Trans. Power Electron.*, vol. 32, no. 3, pp. 1779–1791, Mar. 2017.

[11] S. Inoue and H. Akagi, “A bidirectional isolated DC–DC converter as a core circuit of the next-generation medium-voltage power conversion system,” *IEEE Trans. Power Electron.*, vol. 22, no. 2, pp. 535–542, Nov. 2007.

[12] B. Zhao, Q. Yu, and W. Sun, “Extended-phase-shift control of isolated bidirectional DC–DC converter for power distribution in microgrid,” *IEEE Trans. Power Electron.*, vol. 27, no. 11, pp. 4667–4680, Nov. 2012.

[13] H. Bai, Z. Nie, and C. C. Mi, “Experimental comparison of traditional phase-shift, dual-phase-shift, and model-based control of isolated bidirectional DC–DC converters,” *IEEE Trans. Power Electron.*, vol. 25, no. 6, pp. 1444–1449, Jun. 2010.

[14] J. Huang, Y. Wang, Z. Li, and W. Lei, “Unified triple-phase-shift control to minimize current stress and achieve full soft-switching of isolated bidirectional DC–DC converter,” *IEEE Trans. Ind. Electron.*, vol. 63, no. 7, pp. 4169–4179, Jul. 2016.

[15] N. Hou, W. Song, and M. Wu, “Minimum-current-stress scheme of dual active bridge DC–DC converter with unified phase-shift control,” *IEEE Trans. Power Electron.*, vol. 31, no. 12, pp. 8552–8561, Dec. 2016.

[16] B. Zhao, Q. Song, and W. Liu, “Efficiency characterization and optimization of isolated bidirectional DC–DC converter based on dual-phase-shift control for DC distribution application,” *IEEE Trans. Power Electron.*, vol. 28, no. 4, pp. 1711–1727, Apr. 2013.

[17] J. Hiltunen, V. Väisänen, R. Juntunen, and P. Silventoinen, “Variable-frequency phase shift modulation of a dual active bridge converter,” *IEEE Trans. Power Electron.*, vol. 30, no. 12, pp. 7138–7148, Dec. 2015.

[18] R. A. Abramson, S. J. Gunter, D. M. Otten, K. K. Afridi, and D. J. Perreault, “Design and evaluation of a reconfigurable stacked active bridge DC–DC converter for efficient wide load range operation,” *IEEE Trans. Power Electron.*, vol. 33, no. 12, pp. 10428–10448, Dec. 2018.

[19] Y. Shen, H. Wang, A. Al-Durra, Z. Qin, and F. Blaabjerg, “A bidirectional resonant DC–DC converter suitable for wide voltage gain range,” *IEEE Trans. Power Electron.*, vol. 33, no. 4, pp. 2957–2975, Apr. 2018.

[20] Y. P. Chan, K. H. Loo, M. Yaqoob, and Y. M. Lai, “A structurally reconfigurable resonant dual-active-bridge converter and modulation method to achieve full-range soft-switching and enhanced light-load efficiency,” *IEEE Trans. Power Electron.*, vol. 34, no. 5, pp. 4195–4207, May 2019.

[21] Z. Qin, Y. Shen, P. C. Loh, H. Wang, and F. Blaabjerg, “A dual active bridge converter with an extended high-efficiency range by DC blocking capacitor voltage control,” *IEEE Trans. Power Electron.*, vol. 33, no. 7, pp. 5949–5966, Jul. 2018.

[22] Y. Xuan, X. Yang, W. Chen, T. Liu, and X. Hao, “A novel NPC dual-active-bridge converter with blocking capacitor for energy storage system,” *IEEE Trans. Power Electron.*, to be published, doi: 10.1109/TPEL.2019.2898454.

[23] G. Ortiz, L. Fässler, J. W. Kolar, and O. Apeldoorn, “Flux balancing of isolation transformers and application of ‘The Magnetic Ear’ for closed-loop volt–second compensation,” *IEEE Trans. Power Electron.*, vol. 29, no. 8, pp. 4078–4090, Aug. 2014.

[24] A. Rodrıguez, A. Vazquez, D. G. Lamar, M. M. Hernando, and J. Sebastian, “Different purpose design strategies and techniques to improve the performance of a dual active bridge with phase-shift control,” *IEEE Trans. Power Electron.*, vol. 30, no. 2, pp. 790–804, Feb. 2015.

Peng Liu received the B.S. and Ph.D. degrees in electrical engineering from the Huazhong University of Science and Technology, Wuhan, China, in 2013 and 2018, respectively.

He is currently a Postdoctoral Research Fellow with the Department of Control Science and Engineering, Huazhong University of Science and Technology. His research interests include three-level dc/dc converters, three-level NPC inverter, PLL technique, and the control strategy of parallel inverters.

Shanxu Duan (M’14–SM’16) received the B.S., M.S., and Ph.D. degrees in electrical engineering from Huazhong University of Science and Technology, Wuhan, China, in 1991, 1994, and 1999, respectively.

Since 1991, he has been a Faculty Member with the School of Electrical and Electronics Engineering, Huazhong University of Science and Technology, where he is currently a Professor. His research interests include stabilization, nonlinear control with application to power electronic circuits and systems, fully digitalized control techniques for power electronics apparatus and systems, and optimal control theory and corresponding application techniques for high-frequency pulsewidth modulation power converters.

Dr. Duan is a Senior Member of the Chinese Society of Electrical Engineering and a Council Member of the Chinese Power Electronics Society. He was selected as one of the New Century Excellent Talents by the Ministry of Education of China in 2007. He was also the recipient of the honor of “Delta Scholar” in 2009.